PAPER

Check for updates

Enhanced performance of biobased composite films: the role of boron nitride nanoplatelets in tuning their hydrophobic, chemical resistance, thermal and electrical properties

Bitupan Mohan, [ab] Rahul Sonkar, [ab] Mridusmita Barman[a] and Devasish Chowdhury *[ab]

The development of sustainable biodegradable polymers or biopolymer-based composites is vital for addressing environmental challenges posed by petroleum-derived materials. However, the practical applications of biopolymers remain constrained by the poor mechanical strength, low chemical stability and poor thermal conductivity. In this study, a multifunctional bio-composite film with excellent mechanical strength and enhanced hydrophobicity was fabricated by incorporating exfoliated boron nitride nanoplates (BNNPs) and cellulose nanofibers (CNFs) into the chitosan (CH) matrix. The influence of BNNP loading on the structural, thermal and surface properties of the film was systematically investigated. Increasing the loading of BNNPs alters the wettability of the resulting films, while significantly enhancing their mechanical strength, thermal stability, and UV shielding performance. At an optimum BNNP loading of 2 wt%, the composite film achieved a tensile strength of 46.3 MPa (an $\sim 82\%$ increase relative to the CH–CNF film), enhanced hydrophobicity with a contact angle of $117.1°$ and a thermal conductivity of 0.68 W m^{-1} °C. The film also demonstrated excellent resistance to acidic and alkaline environments. Structural and morphological analyses confirmed uniform dispersion of BNNPs and strong interfacial interaction with CNFs, promoting effective stress transfer and phonon transport. Furthermore, the bio-composite film displayed sensitivity towards ammonia (NH$_3$), showing a decrease in resistance as observed in Cole–Cole plots upon exposure to ammonia, depicting improved charge transfer. These findings highlight the synergistic role of BNNPs and CNFs in engineering high-performance, eco-friendly films suitable for packaging, protective coatings, and flexible electronics as well as the film's potential for ammonia sensing applications.

1. Introduction

The development of biopolymer-based composites has gained significant attention due to the growing demand for sustainable, biodegradable, and high-performance materials.[1] With increasing environmental concerns regarding the excessive use of petroleum-based plastics, which contribute to pollution and ecological imbalance, there is an urgent need to develop eco-friendly alternatives.[2] Biopolymer-based composites offer a promising solution, as they are derived from renewable sources, reduce dependency on fossil fuels, and have the potential to degrade naturally, minimizing environmental

impacts.[3,4] However, biopolymers, despite their widespread application, often suffer from poor mechanical strength, limited chemical resistance, and low thermal conductivity, restricting their usability in advanced applications such as packaging, electronics, and protective coatings.[2] Similar to many petroleum-based polymers, the properties of traditional biopolymers can also be enhanced through blending and composite formation. The integration of reinforcing agents, fillers, or nanoparticles into biopolymers enables the development of composites with improved mechanical characteristics, barrier properties, thermal stability, and broader functional capabilities, making them suitable for diverse industrial uses.[5,6]

There is increasing interest in combining biopolymers with nanofillers, which have different shapes and nanoscale dimensions with the individual particle size within the range of 1–100 nm.[5–7] Their small size provides a high surface area, enhancing the interaction between the biopolymer matrix and the nanofiller. This interaction can significantly improve the

[a] *Material Nanochemistry Laboratory, Physical Sciences Division, Institute of Advanced Study in Science and Technology, Paschim Boragon, Garchuk, Guwahati-781035, Assam, India. E-mail: devasish@iasst.gov.in; Fax: +91 361 2279909; Tel: +91 361 2912073*

[b] *Academy of Scientific and Innovative Research (AcSIR), Ghaziabad-201002, India*

mechanical, thermal, chemical and barrier properties of bio-nanocomposite materials.[8,9] Many researchers have explored various types of organic, inorganic and carbon nanofillers such as metals, metal oxide nanoparticles, graphene, graphene oxide, carbon nanotubes, nanocellulose, *etc.* for incorporation into biopolymer matrices with a focus on improved functional properties of nanocomposite materials.[8,10–13] Among them, two-dimensional (2D) graphene-based nanofillers, which are highly oriented structures, have been most widely studied in different biopolymer matrices due to their excellent mechanical, electrical, optical, thermal and biomedical properties.[12,14] Similar to graphene, hexagonal boron nitride (hBN), also known as "white graphene," has emerged as a promising lamellar material.[15] It offers exceptional mechanical strength, high thermal conductivity, excellent chemical and thermal stability, insulating properties, inherent hydrophobicity, and a low thermal expansion coefficient.[15,16] Owing to these remarkable properties, h-BN and its platelet form (BNNPs) are considered ideal candidates for enhancing the performance of biopolymer-based films to improve the thermal conductivity, lubricity, flame retardancy, and dielectric properties.[17–19] In addition to graphene-based and h-BN nanofillers, cellulose nanofibers (CNFs) have also gained attention as a reinforcing material in biopolymer composites.[20] Derived from renewable resources such as wood pulp, agricultural residues, and bacterial cellulose, CNFs exhibit exceptional mechanical strength, lightweight characteristics, and biodegradability, making them an attractive choice for sustainable material development.[21–23] Their high aspect ratio, large surface area, and abundant hydroxyl functional groups facilitate strong interactions with polymer matrices, leading to enhanced mechanical properties, improved thermal stability, and superior barrier performance.[24,25] Moreover, CNFs contribute to the formation of dense, entangled networks within the polymer matrix, reducing gas permeability and increasing moisture resistance. Due to these advantages, CNFs are widely explored for applications in packaging, coating, sensing and biomedical fields.[26–28] When combined with other advanced nanomaterials such as hBN, they enable the fabrication of hydrophobic, thermally conductive, and chemically resistant composite films, effectively overcoming the inherent limitations of conventional biopolymer-based materials.[29,30]

Several studies have demonstrated the potential of h-BN, CNFs, and biopolymer-based composites in enhancing mechanical, thermal, and barrier properties. For instance, BNNP-reinforced polyvinyl alcohol (PVA) films have shown significant improvements in thermal conductivity, making them suitable for heat management applications.[31] Similarly, CNF/gelatin composite films have exhibited enhanced flexibility and biocompatibility, making them promising materials for biomedical applications such as wound dressings and tissue engineering scaffolds.[32,33] Chitosan, a widely studied biopolymer, has been incorporated with various nanofillers to develop functional composite films with antimicrobial, biodegradable, and high-strength properties.[34] Chitosan–BNNP nanocomposites have been reported to enhance thermal stability and

improve barrier performance, making them suitable for food packaging applications.[35] Additionally, cellulose/chitosan network hydrogels demonstrate remarkable mechanical reinforcement, stretchability and self-healing alongside excellent biocompatibility and significantly accelerated wound healing of skin defects.[36] Despite extensive research on reinforcing biopolymer films with nanomaterials, several critical challenges remain unresolved. One of the key limitations is the inherently low thermal conductivity of biopolymers (~ 0.1 W m^{-1} K^{-1}), which restricts their applications in electronics and thermal management systems.[37] Additionally, conventional biopolymer films are highly susceptible to environmental factors such as moisture absorption and chemical degradation. Their tendency to absorb water leads to swelling, mechanical deterioration, and a reduced lifespan, while exposure to acidic, alkaline, or organic solvents accelerates their degradation.[38] The incorporation of BNNPs can significantly enhance heat dissipation, making the composite film suitable for flexible electronics, heat spreaders, and thermally stable coatings.[15,18,39] Since BNNPs inherently repel water, their proper dispersion within the polymer matrix can significantly enhance both moisture resistance and chemical stability. This research aims to explore the combined effects of BNNPs and CNFs in enhancing the film's durability in harsh environments. BNNPs have been widely studied for their ceramic-like thermal conductivity, oxidation resistance, and hydrophobic behavior.[40,41] However, their poor dispersion in polymer matrices limits their potential benefits.[42] In contrast, CNFs provide excellent interfacial adhesion within biopolymer networks, improving mechanical integrity and facilitating the uniform dispersion of nanofillers.[27] By carefully engineering the structure and dispersion of these nanomaterials, the resultant BNNP/CNF–biopolymer composite film is anticipated to achieve an optimal balance of strength, durability, and environmental sustainability.

In this study, we report the fabrication and detailed characterization of a biopolymer-based nanocomposite film incorporating boron nitride nanoplatelets (BNNPs) and cellulose nanofibers (CNFs) into a chitosan matrix. This hybrid system was strategically engineered to address the limitations of traditional biopolymer films by improving their thermal, mechanical, and chemical resistance performance. CNFs, extracted from banana fibers, serve as biodegradable structural reinforcements, while BNNPs provide hydrophobicity, chemical durability, and high thermal conductivity. The combined incorporation of these nanofillers is designed to create a composite film with enhanced surface morphology, mechanical robustness, chemical resistance, and thermal performance. We also tested the capability of the composite film for the detection of NH$_3$ solution at room temperature using the electrochemical impedance spectroscopy (EIS) sensing method (Cole–Cole plot). The comprehensive analysis of wettability, thermal conductivity, degradation resistance, and dielectric behavior presented in this work underscores the film's potential for advanced applications in eco-friendly packaging, thermal insulation, moisture-resistant coatings and ammonia sensing.

2. Experimental

2.1. Materials and chemicals

Chitosan of medium molecular weight (CAS: 9012-76-4) was obtained from Sigma-Aldrich. Boron nitride nanopowder with an average particle size of 70 nm and isopropanol (IPA, 99.5%) were purchased from SRL, India. Acetic acid (glacial, 100%), hydrogen peroxide (H_2O_2, 30%), ammonia solution (25%), sulfuric acid and sodium hydroxide (NaOH) were procured from Merck. Banana plant (*Musa balbisiana*) fibers were collected from the Institute of Advanced Study in Science and Technology (IASST), Guwahati campus, and used as a natural cellulose source. All chemicals were of analytical grade and were used without any further purification. Throughout the study, distilled water was used as the primary solvent for all solution preparation and washing steps.

2.2. Preparation of exfoliated h-BN (BNNPs)

Boron nitride nanoplatelets (BNNPs) were prepared from bulk BN nanopowder (average particle size $\sim$ 70 nm) through a liquid-phase exfoliation process assisted by ultrasonication. In a typical procedure, 1 g of bulk BN nanopowder was sonicated in 500 mL of a 1:1 (v/v) isopropanol (IPA) and deionized water (DI-H_2O) mixture. The dispersion was subjected to ultrasonication using a probe sonicator at 40% intensity with a tip diameter of 13 mm, maintaining a temperature cutoff of 60 °C. The sonication was performed for 2 h in pulse mode (5 s on and 8 s off) to ensure effective exfoliation. Following the ultrasonication, the resulting stable suspension of BNNPs was centrifuged at 5000 rpm for 15 min. The supernatant containing exfoliated BNNPs was collected, washed multiple times with deionized water, and subsequently dried at 80 °C overnight to obtain the final BNNP powder.

2.3. Preparation of cellulose nano-fibrils from banana fibers

To prepare the cellulose nanofiber (CNF), first banana pseudo-stems were harvested, and each sheath was carefully separated. The sheaths were then fed into a decorticator machine to extract the fibers, which were then dried and stored. After this the fibers were cut into 2 mm snippets using a cutter mill before undergoing degumming. A two-stage process for removing gum and non-fibrous materials was performed in a 2000 mL beaker vessel placed in a fume hood. To maintain uniformity in the bath, the mixture was stirred at regular intervals. The banana fibers were treated with 5% NaOH for 1 hour at 80 °C, then rinsed with dilute acetic acid to neutralize the solution and dried in the fume hood. Bleaching was carried out with 0.3% H_2O_2 and sodium silicate (10 g L^{-1}) at 80 °C for 1 hour, maintaining a pH of 10. The fibers were then rinsed, neutralized, and dried.

Treated banana fibers (10 g) were mixed with 1000 mL of hot water (1% dry cellulose) and blended mechanically, followed by heating at 80–100 °C for 30 minutes. The cooled mixture was shear-homogenized using an IKA T-25 Ultra-Turrax at 13 000 rpm for 1 hour and then passed through a GEA high-pressure homogenizer (900 bar, 5 passes). The resulting CNFs were stored for further use and characterization.

2.4. Fabrication of CH–CNF–BNNP films

Different nanocomposite films as well as pure chitosan (CH) and CNF films were prepared by a solvent casting method. Firstly 0.02 g mL^{-1} chitosan solution was prepared by dissolving 0.2 g of chitosan in 10 mL of 0.1 M aqueous acetic acid. This chitosan solution was added to the 10 mL 1% CNF solution, and a homogeneous solution was made by stirring at 600 rpm on a magnetic stirrer overnight at room temperature. The BNNP suspension was prepared by dispersing different amounts of boron nitride in water with sonication for 1 h and then gradually added to the chitosan-CNF dispersed solution, followed by stirring at 600 rpm at ambient temperature for 24 h. This solution mixture was sonicated on a bath sonicator for 1 h for degassing. After degassing, the solution was cast on a 100 mm diameter Teflon plate and dried in a hot air oven at 50 °C for approximately 17 h. The dried film was peeled out from the Teflon plate and stored in a vacuum. During the fabrication of the films, 45 mL of the total volume of the mixture was maintained. According to the mass fraction, different amounts (0.5, 1, 2, and 3 wt%) of BNNP incorporated CH–CNF–BNNP composite films were labelled as BN0.5, BN1, BN2, and BN3 respectively.

2.5. Chemical stability test

The chemical stability of the films was tested against acidic and basic aqueous media. A separate beaker was filled with 40 mL of hydrochloric acid (1 M) and NaOH (1 M). First, the samples were cut into 1×1 cm^2 dimensions and dried in a hot air oven at 55 °C to remove all the moisture until a constant weight was achieved. Then, the samples were immersed in the respective solution for a period of 7 days. After collecting the samples from each solution, excess solvents were removed from their surface using a blotting paper and the weight of the samples was recorded. Similarly, to evaluate the mechanical properties of the prepared film after acid and base treatments, samples were cut into 1×7 cm^2 dimensions and soaked in 40 mL of acidic and basic aqueous media. The percentage of weight loss was calculated by using eqn (1).

$$\text{Weight loss (\%)} = \frac{W_i - W_f}{W_i} \times 100 \qquad (1)$$

where W_i is the dry weight of samples before immersing in acidic and basic media and W_f is the dry weight of samples after immersing in acidic and basic media.

2.6. Measurement of dielectric properties

The dielectric properties of the composite film were systematically examined using an LCR meter over a broad frequency range of 4 Hz to 8 MHz at a temperature of 300 K. For precise and reliable measurements, the films were cut into 1×1 cm^2 samples, as detailed in the SI of this article. Silver paste was applied to both sides of each sample to ensure optimal electrical contact. Additionally, Cole–Cole plots were employed to

evaluate the ammonia sensing performance of the BN2 composite film.

2.7. Characterization

The synthesized nanomaterials and nanocomposite films were characterized using various analytical techniques. Fourier Transform Infrared (FTIR) spectroscopy was performed using a PerkinElmer spectrum FTIR instrument by the ATR method in the spectral range of 4000–400 cm^{-1}. X-ray diffraction (XRD) analysis was conducted using a Bruker D8 Advance X-ray diffractometer (Karlsruhe, Germany) with Cu Kα radiation ($\lambda = 1.54056$ Å) at a scan rate of 1.5 s per step over an angular range of $2\theta = 5°–80°$. The operating conditions of the XRD tube were maintained at 40 mA and 40 kV. The optical properties of the nanomaterials and nanocomposite films were analyzed using a Shimadzu UV-2600 spectrophotometer. Transmission electron microscopy (TEM) was carried out with a JEOL TEM-2100 instrument (Tokyo, Japan) to examine the morphology and SAED pattern of the prepared BNNPs and CNFs. The surface morphology and elemental composition of the nanomaterials and composite films were investigated using a SIGMA VP (ZEISS) scanning electron microscope (SEM) (Oberkochen, Germany) equipped with an energy-dispersive X-ray (EDX) spectroscopy unit. The thermal stability of the films was evaluated using a PerkinElmer 4000 thermogravimetric analyzer (TGA) at a nitrogen flow rate of 20 mL min^{-1}, within a temperature range of 35–800 °C, at a heating rate of 10 °C min^{-1}. Prior to analysis, approximately 5–10 mg of each sample was cut into small pieces and dried overnight in a vacuum oven. The mechanical properties of the films were assessed using a universal testing machine (Tinius Olsen 5ST) at a testing speed of 20 mm min^{-1}. The load cell capacity and gauge length were set to 2.5 kN and 20 mm, respectively, following the ASTM D638 standard. Film thickness was measured using an electronic micrometer (Schut, Germany). The wettability of the composite films was analyzed by measuring the contact angle using the sessile drop method with sterile water at 20 °C. The experiments were repeated at least three times to get results in good agreement with the logical values and were reproducible.

3. Results and discussion

3.1. Characterization of BNNPs and CNFs

Boron nitride based nanocomposites particularly with polymers have been extensively used in thermal management, electrical insulation, lubrication and wear-resistant coating applications due to their exceptional thermal and chemical stability and electrical properties.[15,39] To fabricate the CH nanocomposite film with BNNPs and CNFs by a simple solvent casting technique as illustrated in Fig. 1, h-BN powder was first exfoliated into h-BNNPs by using an ultrasonic probe method. The films were prepared starting from 1% chitosan dissolved aqueous acetic acid solution mixed with a solution of dispersed CNFs and BNNPs of known weight concentration.

As-exfoliated BNNPs were characterized using FT-IR, XRD and micro-Raman, TEM and SEM to investigate the structural characteristics and bonding interactions in comparison to bulk BN. The XRD patterns, presented in Fig. 2(a), reveal the characteristic diffraction peaks corresponding to the h-BN phase. Upon exfoliation into BNNPs, the (002) diffraction peak shifted to a lower angle (26.48°) is observed (as shown in the inset of Fig. 2(a)). The shift towards a lower 2θ value suggests an
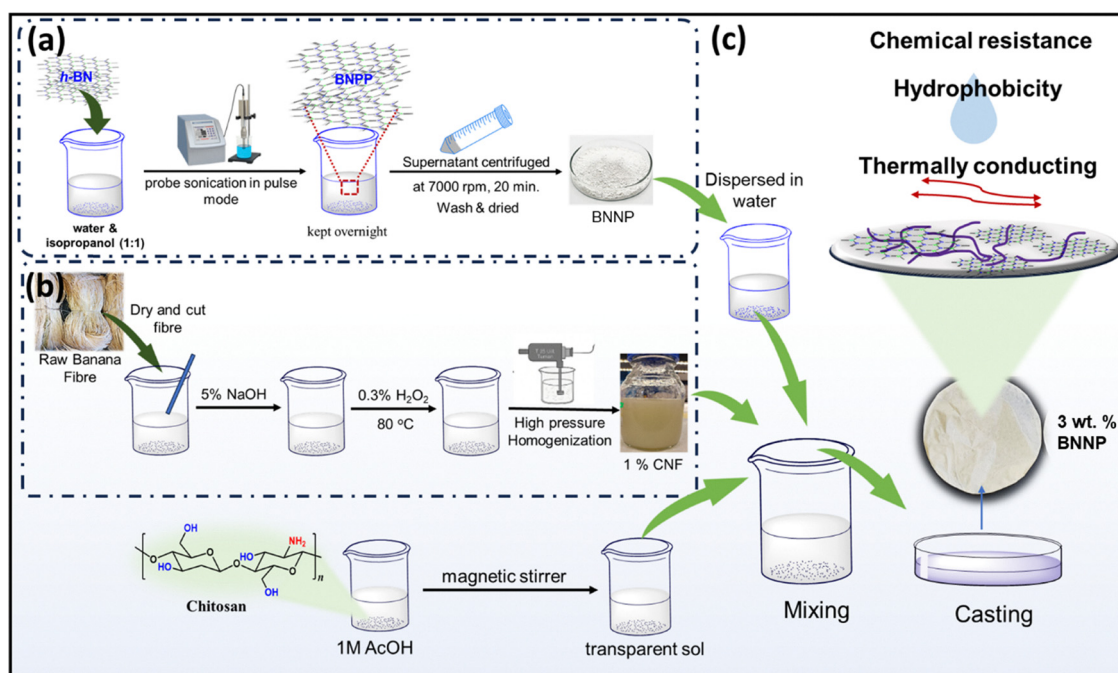

Fig. 1 Schematic illustration of the fabrication process of CH–CNF–BNNP nanocomposite films: (a) exfoliation of bulk h-BN to obtain BNNPs, (b) preparation of cellulose nanofibers (CNFs) from banana fibers and (c) mixing of CH, CNFs, and BNNPs followed by film casting.
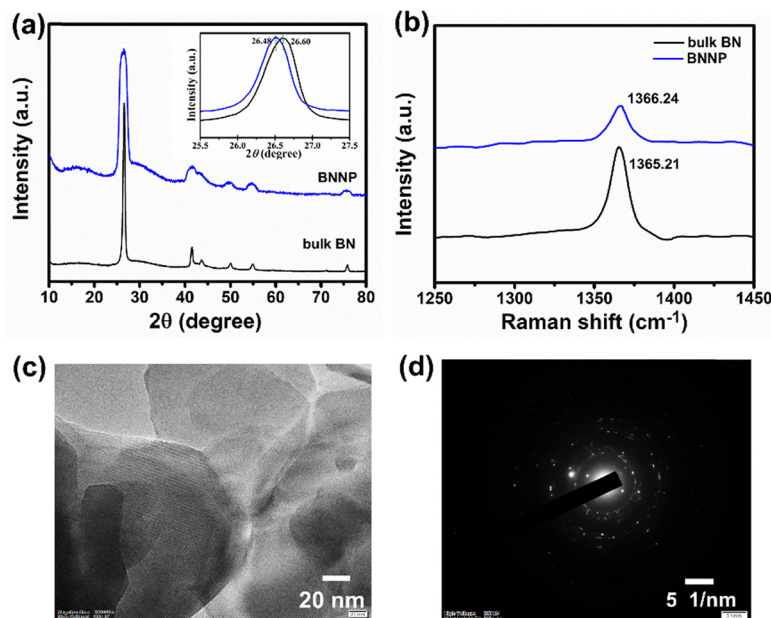
Fig. 2 (a) XRD patterns with the inset showing the (002) peak shift, (b) Raman spectra of bulk h-BN and as-exfoliated BNNPs, (c) TEM image and (d) selected area electron diffraction (SAED) pattern of exfoliated BNNPs.

increase in the interlayer spacing (*d*-spacing), which is attributed to the weakening of van der Waals interactions between adjacent BN layers.[43,44] Similarly, in Raman spectra, a slight shift in the E_{2g} peak from 1365.21 cm^{-1} for bulk BN to 1366.24 cm^{-1} for BNNPs is observed. This shift can be attributed to the reduction in layer thickness, increased phonon confinement effects, and strain-induced variations in the exfoliated boron nitride nanoplatelets. The broader peak observed in BNNPs suggests a reduction in the crystallite size and increased disorder, which is commonly observed in exfoliated or nanoscale h-BN structures.[43]

Fig. S2 shows the FTIR spectra of bulk BN and exfoliated BNNPs, with two primary characteristic peaks corresponding to the vibrational modes of h-BN. According to the literature,[45] one distinctive and broad transmittance peak was observed at a wavenumber of 1344 cm^{-1}, and this can be attributed to B–N stretching vibration. The other distinctive transmittance peak, which corresponds to the B–N–B bending vibration, was seen at a wavenumber of 767 cm^{-1}. Upon exfoliation, the BNNS spectrum retains the characteristic B–N vibrational modes, indicating that the fundamental B–N bonding remains intact. However, a noticeable broadening in peak intensity is observed in the BNNP spectrum compared to bulk BN. This effect can be attributed to the disruption of interlayer interactions and increased structural disorder due to exfoliation.[43] Furthermore, no additional peaks are observed in the 3200–3500 cm^{-1} range, which confirms the absence of hydroxyl (–OH) or oxidation-related functional groups. This indicates that the exfoliation process did not lead to oxidation or chemical degradation of BNNPs.

SEM and HRTEM analyses were performed to examine the morphological and structural characteristics of bulk h-BN and exfoliated BNNPs at different magnifications and are presented in Fig. S3, S4 and Fig. 2(c), (d). The SEM image of bulk h-BN (Fig. S3(a)) reveals agglomerated clusters with an irregular morphology. The presence of thick and aggregated structures suggests strong interlayer interactions, which are characteristic of bulk h-BN due to its intrinsic van der Waals forces. As displayed in Fig. S3(b)–(d) the SEM images of BNNPs at different magnifications (500 nm, 300 nm, and 200 nm) show more homogeneous, with thin, nanosheet-like structures distributed across the field of view. As the magnification increases, it becomes evident that individual nanosheets have a reduced thickness and increased lateral dimensions, confirming the formation of few-layered BNNPs. Additionally, the reduced agglomeration suggests a decrease in interlayer interactions, which is in agreement with XRD and Raman analyses. Furthermore, the AFM image (Fig. S1) clearly reveals homogeneous nanosheets with lateral dimensions in the nanometer range and an average thickness of approximately 4 to 5 nm, confirming the formation of few-layer BNNPs. The TEM micrograph (Fig. 2(c) and Fig. S4) of BNNPs at different magnifications also shows ultrathin, transparent, and sheet-like morphology, confirming the successful delamination of bulk h-BN into few-layered nanosheets. The HRTEM image in Fig. S4(c) displays well-defined lattice fringes with an interplanar *d* spacing of about 0.317 nm, suggesting a high degree of crystallinity, which is essential for maintaining the intrinsic properties of BNNPs in various applications. The SAED pattern (Fig. 2(d)) shows distinct diffraction rings, confirming the polycrystalline nature of the exfoliated BNNPs.

Fig. 1 illustrates the process involved in extracting cellulose nanofibers (CNF) from banana fibers. The material, initially brown due to the alkaline treatment, turned bright white after

bleaching. During the alkaline treatment, substances like starch, pectins, and hemicelluloses underwent hydrolysis. As for the bleaching process, hydrogen peroxide (H_2O_2) effectively removed the lignin responsible for the banana fiber's brown color. This method, commonly used for lignin removal in plant materials at the lab scale, involves treating the fiber with a hydrogen peroxide solution at pH 10.0 for 1 hour, which removes most of the lignin; however, additional treatment is required to fully bleach the suspension. The snippets obtained after cutter milling were crucial for both the exfoliation and the final size of the fibrils. A 2 mm grid was used for the cutter mill following the preliminary treatment. The open ends of the snippets facilitated defibrillation under shear force, further releasing the nanofibers from the structure.

To evaluate the dimensions of banana fiber derived cellulose nanofibrils, SEM and TEM were employed, and 50 measurements from both high and low magnification images were analyzed for each treatment using ImageJ, as depicted in Fig. 3(a)–(d). SEM analysis, shown in Fig. 3(a), reveals a dense and high interconnected network of fibrillar structures, indicating successful fibrillation of cellulose fibers. The fibers appear uniformly dispersed with minimal aggregation, suggesting efficient defibrillation during the treatment process. The corresponding thickness distribution histogram (Fig. 3(b)) demonstrates an average fibril thickness of approximately 44 nm, consistent with typical nanoscale cellulose structures. TEM imaging (Fig. 3(c)) further confirms the nanoscale nature and high aspect ratio of the CNFs. The image illustrates a web-like network structure with thin and entangled fibrils, which are indicative of complete disintegration of the microfibrils from the cellulose source. The associated thickness distribution analysis (Fig. 3(d)) shows a narrower distribution centered around an average thickness of 35.17 nm, which is slightly lower than that obtained from SEM, possibly due to the higher resolution and contrast capabilities of TEM. Some fibers

appeared larger in the images due to aggregation during sample preparation. Moreover, the sizes were comparable to nanosized structures derived from other sources.[46] AFM topographic images, displayed in Fig. 3(e), showed that cellulose nanofibers have a fibril-like structure. The height profile extracted from AFM with an average thickness of 33 nm (Fig. 3(f)) provides a quantitative measure of the fibril thickness, complementing the observations from SEM and TEM.

Zeta potential measures the electrostatic repulsion between particles due to their surface charges, providing insight into the stability of colloidal suspensions. Dynamic light scattering (DLS) analysis, as depicted in Fig. S5, revealed a size distribution with two peaks, having an average width of 42.68 nm and length of 418.7 nm. The average zeta potential measured for the CNF suspension was −18.4 mV. A negative zeta potential indicates the presence of negatively charged groups on the nanofibers' surfaces. CNF suspensions with negative zeta potential values are considered to have strong stability, as the electrostatic repulsion between similarly charged particles prevents aggregation.

Fourier-transform infrared spectroscopy was employed to analyze the transmittance bands of raw, alkali treated, H_2O_2 treated and cellulose nanofibers (CNFs) derived from banana fibers, as depicted in Fig. 3(g). The spectra revealed characteristic absorption peaks associated with cellulose at approximately 3320 cm^{-1} (O–H stretching), 2900 cm^{-1} (C–H stretching), 1423 cm^{-1} (CH_2 bending), 1028 cm^{-1} (C–O stretching), and 897–900 cm^{-1} (β(1 → 4) glycosidic linkages). These peaks exhibited significant broadening from raw to treated fibers, indicating an increase in cellulose content. The spectra also displayed characteristic absorption peaks of lignin at 1637 cm^{-1} (C=O stretching), 1522 cm^{-1} (aromatic ring vibrations), 1462 cm^{-1} (C–H deformation), and 1249 cm^{-1} (aryl C–O stretching). The intensities of these peaks also diminished after treatment.[47] The peak at 1154 cm^{-1}, associated with vibrations of amorphous materials,
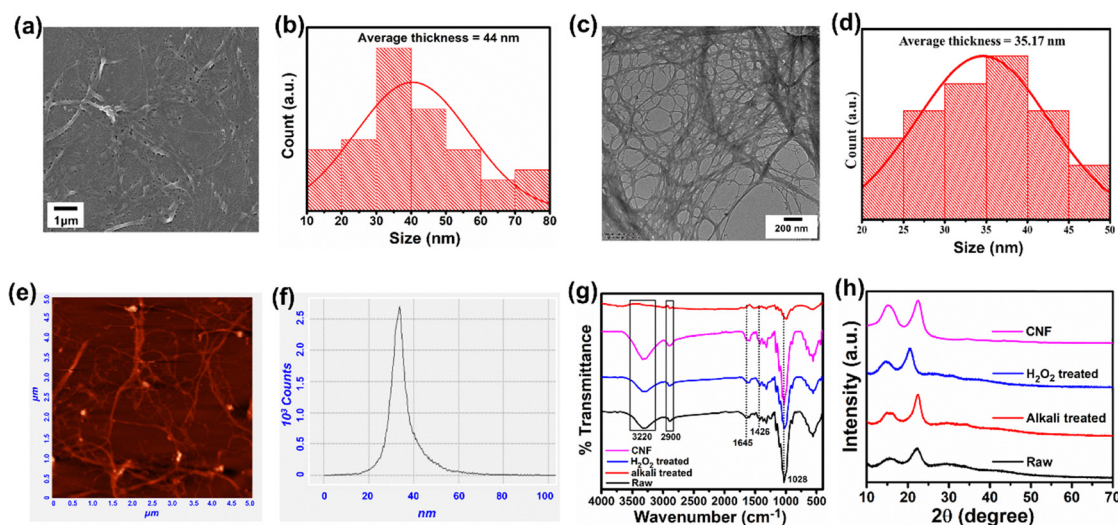

Fig. 3 Morphological and structural characterisation: (a), (c) and (e) present SEM, TEM, and AFM images showing surface topology, and (b), (d), and (f) present their average thickness distributions, respectively, confirming uniform formation of the fibrils; (g) FT-IR and (h) XRD analyses of the raw, alkali treated, peroxide treated and cellulose nano-fibrils.

diminished following peroxide treatment, suggesting an increase in cellulose crystallinity. Furthermore, a peak at 1640 cm^{-1} observed in the spectra of nanofibers and bleached fibers indicates water absorption. Importantly, no new peaks emerged during the nano-fibrillation process, signifying that no additional functional groups were introduced into the CNF surface. These FTIR analyses confirm that the applied treatments effectively increased cellulose content while reducing lignin and hemicellulose in the banana fibers, resulting in highly crystalline cellulose nanofibers.[48]

The impact of homogenizing mechanical treatment on the crystallinity of CNFs was investigated using XRD analysis, shown in Fig. 3(h). The results demonstrated that treated cellulose exhibited higher crystallinity compared to the original banana fibers, primarily due to the partial removal of hemicellulose and lignin during chemical treatment. For raw banana fibers, peaks at approximately 15.4° (broad), 21.9° (broad), and 29.7° (very small) correspond to crystalline planes with Miller indices of 110, 200, and 400, respectively, indicating the presence of cellulose I. The diffraction patterns of the nanofiber samples were comparable, with two broad peaks. The sharper diffraction peaks at 15.5° and 22.1° are typical of cellulose I, indicating the nanofibers' increased crystallinity. These findings suggest that both chemical and mechanical treatments significantly influence the crystallinity of cellulose nanofibers.[49]

3.2. Composite film characterization

Fourier transform infrared spectroscopy (FTIR) was conducted to investigate the functional groups and molecular interactions within the CH–CNF–BNNP composite. The FTIR spectra of CH, CNF–CH, and CNF–CH–BNNP with varying BNNP concentrations are presented in Fig. 4(a). The spectrum of pure CNF film exhibits characteristic absorption bands of O–H stretching vibration as well as inter- and intra-molecular hydrogen boning vibration of cellulose in the wavenumber range 3600–3000 cm^{-1}. The peak located around 2900 cm^{-1} is associated with C–H stretching vibration of the aliphatic methylene group. The characteristic cellulose peaks are evident in the fingerprint region of the spectrum. The band observed near 1640 cm^{-1} is assigned to the O–H bending vibration of adsorbed water molecules, reflecting the hydrophilic nature of CNFs. The presence of a peak at approximately 1430 cm^{-1} corresponds to C–H bending vibrations, while the absorption near 1370 cm^{-1} is attributed to C–H deformation in polysaccharides. The peak at 1160 cm^{-1} is associated with C–O–C asymmetric stretching, a signature of the β-1,4-glycosidic linkages in cellulose, confirming the preservation of the cellulose backbone in the CNF structure.[50] The incorporation of CNFs in chitosan leads to distinct spectral changes, particularly in the fingerprint region (1700–500 cm^{-1}). The amide C=O stretching and amide N–H bending bands of chitosan, appearing around 1646 cm^{-1} and 1550 cm^{-1}, respectively, remain prominent in the composite spectrum. However, a slight shift and intensity variation in these peaks indicate hydrogen bonding interactions between the amine groups of chitosan and the hydroxyl groups of CNFs. Additionally, the peak at 1164 cm^{-1}, corresponding to the C–O–C glycosidic linkage in chitosan, becomes more pronounced upon CNF incorporation, suggesting enhanced intermolecular interactions. Upon incorporation of BNNPs at
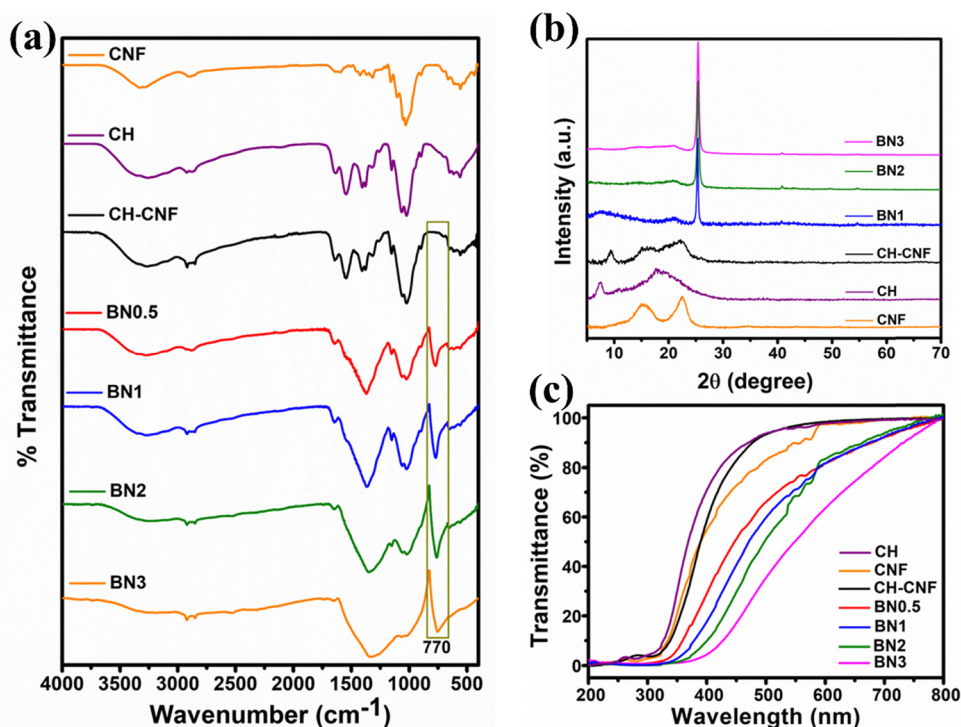

Fig. 4 (a) FTIR spectra, (b) XRD patterns and (c) UV-vis spectra of CNFs, CH and different amounts of BNNP incorporated CH–CNF composite films.

different loadings, new peaks at ~ 1350 cm^{-1} and ~ 778 cm^{-1} correspond to the B–N stretching and bending vibrations respectively, confirming the successful incorporation of BNNPs into the composite. The intensity of these peaks increases as the BNNP concentration increases (from BN0.5 to BN3). The characteristic peaks of CH and CNF at 1650 cm^{-1} and 1580 cm^{-1}, corresponding to amide (C=O stretching) and amide (N–H bending) vibrations, remain evident in all composite spectra. However, after BNNP incorporation, these peaks exhibit shifting and broadening, implying possible structural modifications due to BNNP dispersion.

Fig. 4(b) shows the diffraction pattern of the CNF film with characteristic broad peaks at approximately $2\theta \approx 16°$ and $22°$, which correspond to the amorphous and crystalline cellulose regions, respectively. The CH shows a broad peak around $2\theta \approx 20°$, indicative of the semi-crystalline nature of chitosan. Upon incorporation of CNFs into CH, a shift and intensity change in the characteristic peaks are observed, suggesting improved structural interactions and compatibility between CH and CNFs. The addition of BN into the CH–CNF matrix results in the emergence of a sharp and intense peak around $2\theta \approx 26.7°$, which is attributed to the (002) plane of BNNPs. The intensity of this peak increases with higher BNNP content, indicating successful incorporation and distribution of BN within the CH–CNF matrix. The results confirm that BNNP incorporation alters the hydrogen bonding network, leading to enhanced structural interactions within the CNF–CH matrix. This interaction is expected to influence the mechanical and thermal properties of the composite films, making them suitable for advanced applications.

The optical transmittance of pure chitosan CH, CNF and their composite films with BNNP was evaluated using UV-visible spectroscopy as presented in Fig. 4(c). The transmittance spectra provide insights into the UV shielding efficiency and optical properties of the developed nanocomposite films. As shown in Fig. 4(c), pure CH and CNF films exhibit the highest transmittance across the measured wavelength range, indicating their limited ability to absorb/block UV radiation. The CH–CNF composite shows a slight reduction in transmittance, suggesting improved interaction between CH and CNFs, which enhances light absorption. The introduction of BN nanosheets into the CH–CNF matrix significantly reduces the transmittance, particularly in the UV region (200–400 nm). In the UV-B region (280–320 nm), the nanocomposite films with BN exhibit near-zero transmittance, indicating strong UV-B blocking capability. Within the UV-A region (320–400 nm), the transmittance gradually increases with the wavelength, but films containing BN still maintain significantly lower transmittance compared to CH and CH–CNFs. The addition of BN nanosheets enhances UV shielding properties, making these films promising candidates for UV-protective films, coatings, and packaging materials. The observed trends highlight the tunability of optical properties based on BN content, allowing for the development of materials with tailored UV-blocking performance.

3.3. Surface morphologies of composites and dispersibility of BNNPs

To investigate the surface morphology and cross-sectional structure of the composite films, SEM imaging was performed at different magnifications and is illustrated in Fig. 5. The dispersion and orientation of BNNPs in the CH–CNF matrix play a crucial role in improving performance. In Fig. 5(a), the
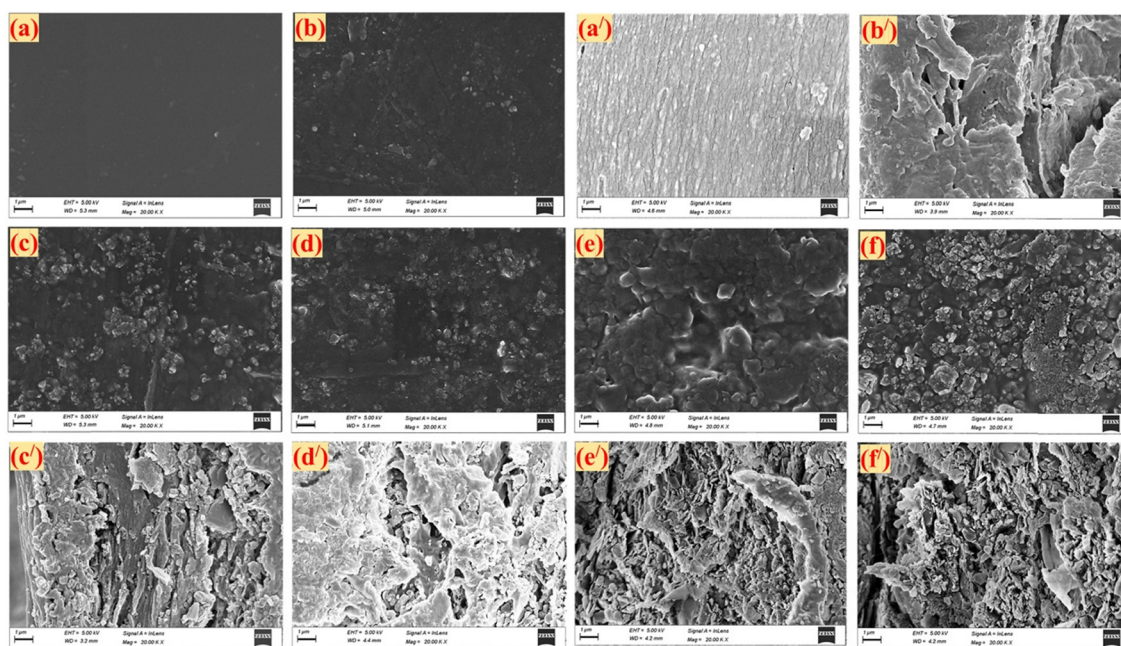

Fig. 5 SEM images showing surface morphology of the (a) pure CH film and (b) CH–CNF composite film, (a′) and (b′) cross-sectional morphology of CH and CH–CNF, respectively, (c)–(f) surface morphology and (c′)–(f′) cross-sectional morphology of BNNP incorporated CH–CNF composite films with increasing weight% of BNNPs of 0.5%, 1%, 2% and 3%, respectively (all scale bars represent 1 μm).

pure chitosan film shows a smooth and homogeneous surface with no discernible porosity or filler particles, indicating a dense film structure typical of neat polymer systems. The addition of CNFs into the chitosan matrix in Fig. 5(b) introduces slight surface roughness, likely due to the entanglement of nanofibers within the chitosan matrix. The cross-sectional image (Fig. 5(a′)) of CH confirms a compact and uniform layered structure, while Fig. 5(b′) shows a more fibrous and network-like structure in the CH–CNF film, indicating interfacial bonding between chitosan and cellulose nanofibers. Upon BNNP incorporation, the surface morphologies change significantly. Fig. 5(c)–(f) show the surface features of BN0.5, BN1, BN2, and BN3 composites, respectively. At a low BNNP content of 0.5 wt% (Fig. 5(c)), the composite surface appears smooth with minimal BNNP aggregation, suggesting a homogeneous dispersion. As the BNNP concentration increases to 1 wt% (Fig. 5(d)), a rougher surface is observed, indicating improved polymer–BNNP interactions. At 2 wt% BNNPs (Fig. 5(e)), distinct nanoparticle clusters are visible, suggesting a saturation limit where additional BNNPs begins to aggregate. In the case of 3 wt% BNNPs (Fig. 5(f)), significant agglomeration is observed, leading to increased surface roughness and potential structural defects. These findings indicate that BNNP concentrations exceeding 2 wt% may result in phase separation, negatively impacting composite homogeneity.

Cross-sectional views in Fig. 5(c′)–(f′) reveal the internal morphology and provide evidence of how BNNPs are distributed within the bulk matrix. The composite film containing 0.5 wt% BNNP (Fig. 5(c′)) exhibits a well-integrated and compact morphology, indicating effective BNNP dispersion within the CNF–CH matrix. At 1 wt% BNNP (Fig. 5(d′)), the composite retains its compact structure with an increase in structural uniformity, suggesting enhanced BNNP–matrix interactions. At 2 wt% BNNP, the cross-section becomes denser, supporting the hypothesis of strong interfacial adhesion. However, at 3 wt% BNNP (Fig. 5(f′)), noticeable crack-like features and voids appear, suggesting that excessive BNNP loading leads to structural inconsistencies, likely due to poor dispersion and phase separation.

SEM analysis confirms that the incorporation of BNNPs influences both surface morphology and internal structure. At optimized concentrations (1–2 wt%), BNNPs are well-dispersed, contributing to a uniform and compact composite structure. However, excessive BNNS loading ($\geq$3 wt%) results in agglomeration, leading to increased roughness, phase separation, and potential defects. These findings suggest that BNNP concentrations within the 1–2 wt% range are optimal for achieving improved mechanical and structural performance in CH–CNF–BNNP composite films.

3.4. Thermal stability, surface wettability and mechanical property analysis

The thermal stability of the nanocomposite films was evaluated using thermogravimetric analysis (TGA) and derivative thermogravimetry (DTGA) under a nitrogen atmosphere at heating rates of 10 °C min^{-1}, as shown in Fig. 6(a) and (b), respectively. The rate of weight loss (%) as a function of temperature provides deeper insights into the decomposition mechanism and thermal stability of the nanocomposite formulations. As demonstrated in Fig. 6(a), the pure CH film exhibits the lowest thermal stability, with significant degradation occurring at lower temperatures (100 °C), indicating its lower resistance to thermal decomposition. The CH–CNF composite shows improved thermal stability compared to CH alone, demonstrating that the
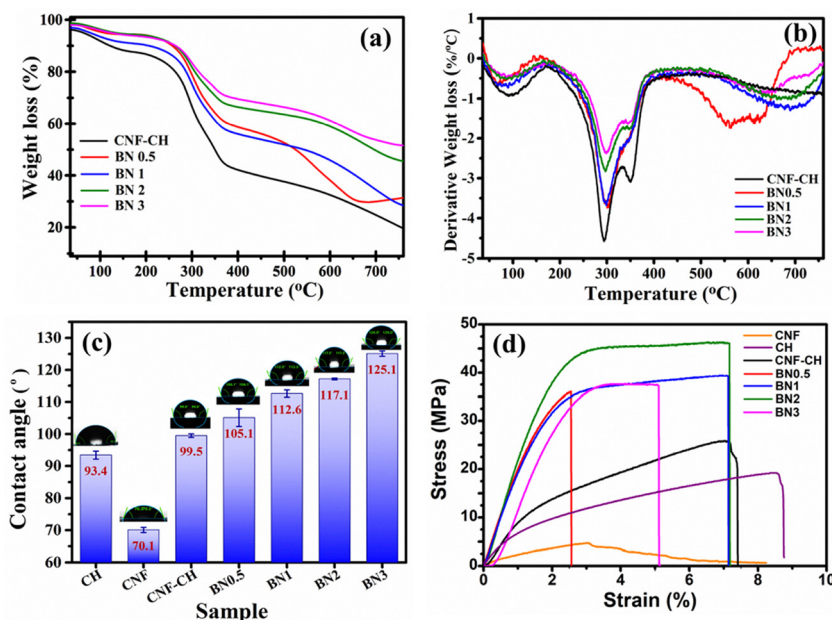

Fig. 6 (a) TGA curves of BNNPs, CH, and different composite films, (b) DTGA curves under a N$_2$ atmosphere, (c) contact angle measurement and (d) tensile stress–strain curves of CH, CNF–CH and different amounts of BNNP incorporated CH–CNF composite films.

incorporation of CNFs enhances the film's resistance to thermal degradation. For the CNF–CH film, the first stage of mass loss is observed up to 120 °C due to the evaporation of remaining 1% dilute acetic acid and water weakly hydrogen-bonded to CH and CNFs. Then, the second stage of decomposition is from 220 to 380 °C, which can be attributed to the complex carbohydrate breakdown process through dehydration due to deamination and depolymerization of CH.[51] The third weight loss occurring above 450 °C resulted from the residual decomposition reactions, during which about 20% weight loss with a total of 19.5% residual weight at 750 °C was observed for the CNF–CH composite film. With the addition of BNNPs, the thermal stability of the nanocomposites further improves. The BNNP incorporated composite film shows a similar three stage degradation; however, the weight loss of the nanocomposites is reduced as the concentration of BNNP increases, with BN3 exhibiting the highest thermal stability. The major weight loss step is observed in the temperature range of 250–400 °C, corresponding to the decomposition of the organic polymer matrix. Beyond this temperature range, residual mass is higher in BNNP-loaded nanocomposites. This enhancement can be attributed to the excellent thermal stability of BNNPs, which slow down the thermal decomposition process by restricting the diffusion of volatile degradation products. The DTGA curves of the film samples also confirm that the thermal stability of the composites improved, as indicated by the shift in the major decomposition temperature towards higher values. Incorporation of 3% BNNP led to the highest decomposition temperature shift to 298.1 °C from 293 °C with no BNNPs in the CH–CNF composite film. The intensity of the DTG peaks also decreases with increasing BN content, indicating a reduction in the decomposition rate. Furthermore, the broad peak at higher temperatures (above 500 °C) is observed for BNNP-loaded nanocomposites, likely due to the slow degradation of the residual carbonaceous structure. The BN3 composite exhibits the lowest weight loss rate, confirming the significant role of BNNP nanoparticles in enhancing thermal stability, making these nanocomposites more suitable for high-temperature applications.

The water contact angle measurement was conducted to evaluate the wettability of the nanocomposite films. As shown in Fig. 6(c), the pure CH and CNF films exhibited lower contact angles of 93.4° and 70.1°, respectively, indicating their hydrophilic nature. However, upon incorporating BNNPs into the CNF–CH matrix, the contact angle significantly increased, reaching 99.5° for CNF–CH and further rising with increasing BNNP content. The BN3 composite exhibited the highest contact angle of 125.1°, demonstrating enhanced hydrophobicity. This improvement can be attributed to the low surface energy and hydrophobic characteristics of boron nitride nanoparticles, which reduce the film's wettability. The increase in the contact angle suggests that the incorporation of BNNPs enhances the water resistance of the composite films, making them suitable for applications where moisture resistance is crucial.

The mechanical performance of the nanocomposite films was evaluated using tensile stress–strain measurements, as shown in Fig. 6(d). The incorporation of CNFs into the chitosan matrix (CH–CNFs) significantly enhanced the mechanical strength due to the reinforcing effect and hydrogen bonding interactions between the chitosan chains and cellulose nanofibers. The CH–CNF composite exhibited a notable increase in both tensile strength to 25.4 MPa and elongation at break compared to pure CH and CNF films. Upon the inclusion of BNNPs into the CH–CNF matrix (BN0.5–BN3), a further enhancement in mechanical strength was observed. The tensile strength of the films increased progressively with increasing BNNP content, reaching a maximum of 46.3 MPa in the BN2 sample. The improvement is attributed to the excellent mechanical stiffness of the BNNPs, which act as nanoscale reinforcements, providing better stress transfer across the matrix and reducing polymer chain mobility. However, at the highest BNNP content (BN3), a slight decrease in tensile strength and elongation was observed. This reduction can be ascribed to BNNP agglomeration, as evidenced in SEM micrographs, which leads to localized stress concentrations and weak interfacial adhesion. Such microstructural discontinuities compromise the overall structural integrity, demonstrating that excessive BNNP loading can be detrimental despite its reinforcing potential.

The fracture morphology of the composite films, as observed in the cross-sectional SEM images (Fig. 5(a′)–(f′)), provides clear microstructural evidence supporting these mechanical trends. The pristine CH film appears as a smooth and featureless fracture surface morphology, indicating a brittle failure with minimal energy absorption. Upon CNF incorporation, the fracture surface seems have rougher and fibrillated cross-sectional morphology, reflecting a shift toward ductile behavior due to effective stress bridging through strong interfacial hydrogen bonding between CNFs and chitosan chains, which hinders crack propagation. Similar CNF-induced stress transfer and pull-out mechanisms have been widely reported in nanocellulose-reinforced biopolymer systems, contributing to enhanced toughness and strength.[52,53] With the addition of BNNPs (Fig. 5(c′)–(f′)), the fracture morphology evolves into a dense, layered morphology, confirming strong filler–matrix interactions. The platelet like BNNPs are uniformly distributed and partially aligned, forming a layered lamellar network that interrupts crack propagation and increasing the fracture energy. The rigid nanoplatelets act as barriers to crack growth while efficiently transmitting stress through the well-adhered CNF–chitosan matrix.[54]

These findings indicate that while the incorporation of BNNPs enhances surface hydrophobicity, it influences the mechanical properties depending on their concentration. The BN2 composite offers a balance between mechanical strength and hydrophobicity, making it a promising candidate for applications requiring both enhanced durability and water resistance.

3.5. Chemical resistance of composite films in alkaline and acidic media

The chemical resistance of the composite films was evaluated by immersing them in 1 M NaOH and 1 M HCl solutions and

their weight loss was monitored (eqn (1) over different time intervals as provided in the Experimental section. This analysis is crucial for assessing the stability and durability of the films in chemically aggressive environments. In practical applications, biomaterial-based composites are often exposed to acidic or alkaline conditions, such as in packaging, biomedical implants, water treatment membranes, and structural materials. Exposure to harsh chemicals can lead to degradation, swelling, or leaching of components, affecting their mechanical strength, barrier properties, and overall performance. By studying the weight loss behaviour, we can determine the extent of chemical degradation, identify the resistance of the material to acidic and alkaline attacks, and evaluate its potential for long-term usability in real-world applications. The percentage of weight loss value of the films after soaking in acidic and basic solutions is graphically represented in Fig. 7(a) and (b). The pure CH and CH–CNF films exhibited significant weight loss in the case of both NaOH treatment and HCl treatment. However, slightly higher weight loss was observed in the acid-treated samples compared to the alkali-treated samples. Strong acids like HCl facilitate the hydrolytic cleavage of glycosidic bonds in CNFs and amide bonds in CH, leading to faster degradation. Also, CH is known to be more soluble in acidic environments due to the protonation of amine groups, making it more susceptible to dissolution in HCl. On the other hand, in an alkaline medium, chitosan remains insoluble but undergoes slow hydrolysis *via* swelling and breakage of hydrogen bonds, which is generally slower than acid hydrolysis. The BNNP-reinforced films showed better stability in both acid and base. The incorporation of BNNPs significantly reduced weight loss, with BN3 exhibiting the least weight loss of 1.8% and 2.8% after 24 h of both base and acid treatments, respectively.

The enhanced acid and base resistance of the BNNP-reinforced films can be attributed to stronger polymer–filler interactions, reduced water uptake, and the shielding effect of BNNPs against acid diffusion. The presence of BNNPs likely reduced the accessibility of hydroxyl ions by forming a protective barrier, thereby improving the structural integrity of the films.

The mechanical and surface properties of the composite films were evaluated after exposure to acidic (1 M HCl) and basic (1 M NaOH) environments for 24 h, and the results are presented as stress–strain curves and contact angle data (Fig. 7(c)–(e)). The overall mechanical performance was better retained in the base-treated films compared to the acid-treated ones. The films containing BNNPs exhibited higher tensile strength values, indicating improved stability under alkaline conditions. This suggests that base treatment causes partial swelling but does not severely degrade the polymer–filler interactions, allowing the films to maintain their structural integrity. However, the stress and strain values after 1 M HCl treatment decreased significantly compared to base-treated films, particularly for CNF–CH and BN0.5 samples. The deterioration in mechanical strength is attributed to acid-induced hydrolysis of CH and CNF components, leading to weaker film structures. Films with higher BNNP loading (BN2 and BN3) showed better mechanical retention, likely due to stronger filler–polymer interactions that resist acid degradation.

The contact angle measurements (Fig. 7(e)) indicate changes in the films' hydrophobicity after chemical exposure. Base-treated films retained relatively higher contact angles compared to the acid-treated ones, suggesting reduced surface wettability due to structural reorganization and partial removal of hydrophilic components under alkaline conditions. Acid-treated films, however, showed a more pronounced reduction
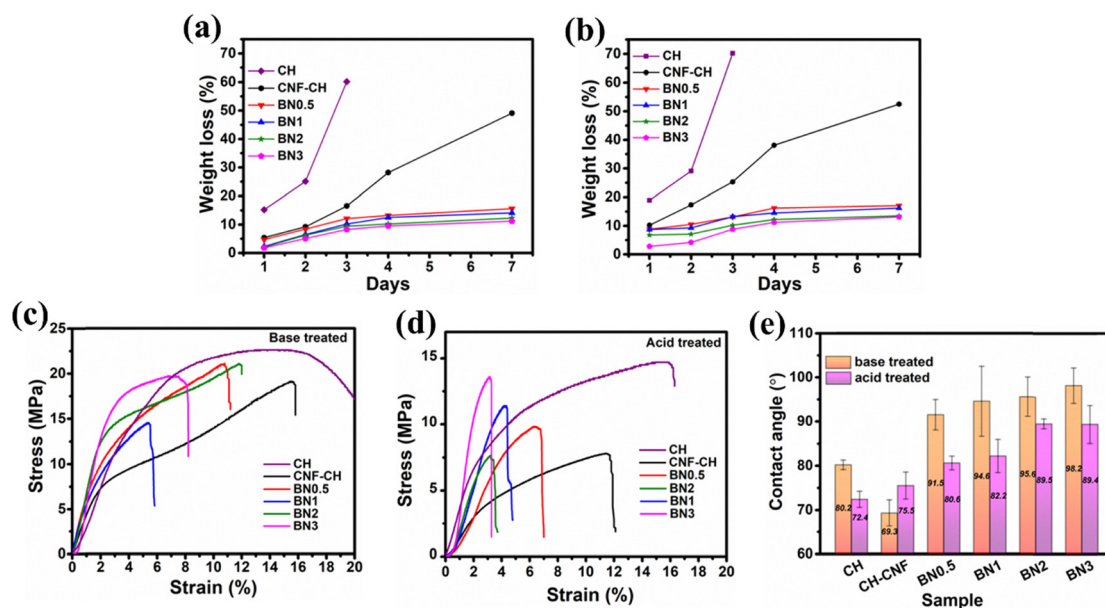

Fig. 7 Percentage of weight loss of different nanocomposite films after soaking in (a) acidic (HCl) solution and (b) basic (NaOH) solution for a period of 7 days. Stress *vs.* strain graphs of nanocomposite films after soaking in (c) basic solution and (d) acidic solution. (e) Contact angle measurements after soaking in basic and acidic solutions.

in the contact angle, indicating increased hydrophilicity due to hydrolytic degradation and leaching of hydrophobic components under acidic conditions. Films with higher 1%, 2% and 3% BNNP contents (BN1, BN2, and BN3) retained relatively high contact angles even after acid treatment, indicating the role of BNNPs in enhancing chemical resistance and reducing water affinity.

Furthermore, the morphological and chemical structures of the films after 24 h of acid and base treatments were examined using FTIR and SEM analyses. The FTIR spectra (Fig. S6(A)) reveal distinct differences in chemical stability between CH–CNF and BN2 films after acid and base treatments. The acid and base-treated CH–CNF films show a marked reduction in N–H bending (~ 1550 cm^{-1}) bands, along with the weakening of the C–O–C stretching (~ 1070 cm^{-1}), indicating hydrolysis and partial deacetylation of chitosan chains. The broadening of the –OH/NH stretching region (~ 3400 cm^{-1}) further confirms hydrogen bond disruption and structural degradation under both conditions. In contrast, the BN2 films exhibit minimal spectral changes, with the main chitosan and cellulose peaks remaining stable and the B–N (~ 1367 cm^{-1}) and B–N–B (~ 787 cm^{-1}) vibrations clearly visible. This stability confirms the chemical inertness of BNNPs and their role as protective barriers, preventing acid–base diffusion and preserving the polymer's functional groups.

The corresponding SEM micrographs provide complementary morphological evidence. The base-treated CH–CNF film (Fig. S6(B)) shows surface erosion and microcracks, indicating severe chemical degradation. In contrast, the base-treated BN2 film (Fig. S6(C)) appears smooth and compact and with an intact surface with no significant cracks, confirming that the presence of BNNPs effectively reinforces structural integrity and resists alkaline etching. Similarly, the acid-treated CH–CNF

surface (Fig. S6(D)) displays clear signs of surface erosion and a porous SEM micrograph, whereas the acid-treated BN2 film (Fig. S6(E)) remains densely packed with a uniform distribution of BNNPs, and no major disintegration is observed.

Overall, the results indicate that the BNNP-reinforced CNF–CH composite films exhibit superior chemical resistance under both acidic and alkaline conditions, making them potential candidates for applications requiring high chemical stability, such as packaging, biomedical coatings, and protective barriers.

3.6. Thermal and dielectric properties of composite films

The temperature-dependent thermal conductivity (k) of CH, CH–CNF, and CH–CNF–BN (0.5, 1, 2, and 3%) was measured using the transient plane source technique over the temperature range of 20 °C to 80 °C. Fig. 8(a)–(c) presents a comprehensive evaluation of the thermal conductivity of CH–CNF and CH–CNF–BNNP composites with varying BNNP concentrations. As shown in Fig. 8(a), the thermal conductivity of all composite films increases with rising temperature across the range of 20–80 °C Notably, the BN3 sample demonstrates the highest thermal conductivity, reaching up to 0.75 W m^{-1} °Cv at 80 °C. This significant enhancement is attributed to the high intrinsic thermal conductivity of BNNPs and their uniform dispersion within the CH–CNF matrix, which facilitates more efficient phonon transport pathways. The increase is consistent across BNNP loading levels, with thermal conductivity rising proportionally with BNNP content. In Fig. 8(b), the specific heat (C_p) of CH–CNF–BN composite films is shown to be lower than that of CH and CH–CNF due to the effect of the nanostructure of materials. The reduction in specific heat may be ascribed to the restricted molecular mobility and lower vibrational degrees of freedom within the nanostructured composite framework. The lower specific heat indicates that the substance required
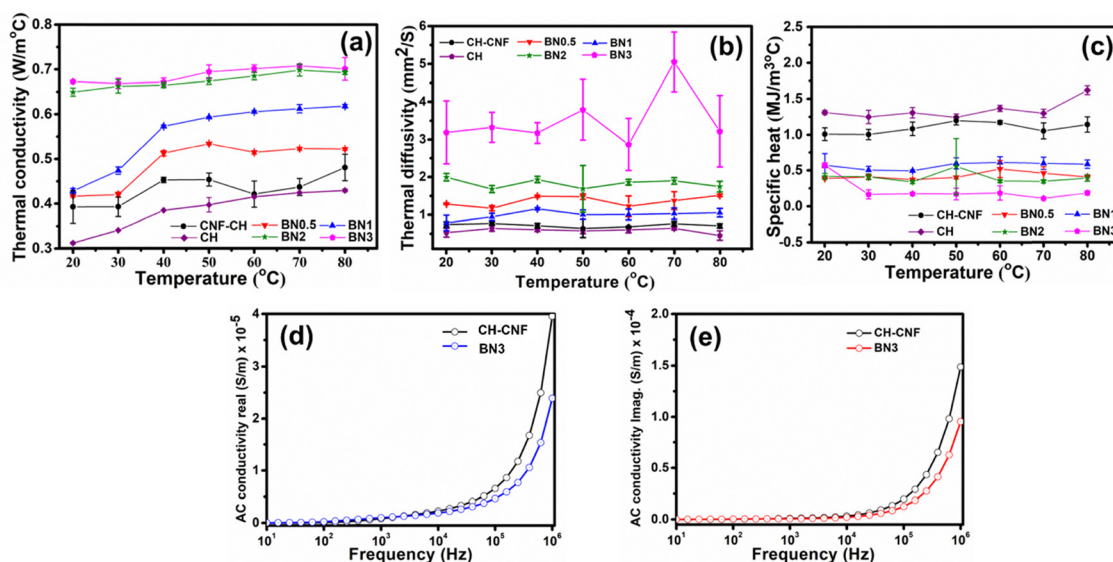

Fig. 8 Temperature-dependent (a) thermal conductivity, (b) thermal diffusivity, and (c) specific heat of CH, CH–CNF, and different amounts of BNNP (0.5, 1, 3, and 5%) incorporated CH–CNF composite films, (d) frequency-dependent real part and (e) imaginary part of AC conductivity for CH–CNF and BN3 films measured at room temperature.

less heat energy to increase its temperature. The variations in specific heat across different composite types remain modest, indicating that BNNP loading primarily enhances heat transport through structural and interfacial effects but does not markedly alter the bulk heat capacity. The thermal diffusivity, which measures the rate of heat transfer through a material, is illustrated in Fig. 8(c). The diffusivity of BNNP incorporated composite films is higher as compared to that of CH and CH–CNF, indicating more heat spreading within the matrix. This enhancement results from the interfacial area as well as surface-to-volume characteristics introduced by BNNP incorporation. At higher temperatures, the combined effects of greater thermal conductivity and decreased specific heat contribute to the overall enhancement of diffusivity. Mechanistically, in non-metallic materials, phonons, *i.e.*, the quantized lattice vibrations, act as the main heat carriers. In composite films, improved phonon transport networks facilitated by the uniform and partial dispersion of BNNPs within the polymer matrix result in an improvement in thermal conductivity. When CNFs and BNNPs are added to the composite, CNFs and BNNPs open up new phonon transfer channels. CNF components enhance interfacial connection within the CH matrix and promote heat transfer because of their high aspect ratio and ordered fibrous network. Further intensifying this effect is BNNPs, which are renowned for their superior heat conductivity because of their layered structure with strong interatomic connections and provide new continuous heat transport pathways. The synergistic effect between the CNF framework and the BNNP fillers results in a well-connected phonon network, enabling superior thermal conduction throughout the composite structure.[55]

To gain further insights into the electrical behavior of the composite films, the AC conductivity of CH–CNF and BN3 composite films was investigated at room temperature using impedance spectroscopy. Both the real and imaginary components of AC conductivity were analysed to understand the influence of BNNP incorporation on the dielectric properties and charge transport mechanisms within the polymer matrix. As expected, the CH–CNF composite films exhibited inherently low AC conductivity due to the insulating nature of both chitosan and cellulose nanofibers. These biopolymers are known for their high resistivity, which makes them suitable for applications requiring dielectric integrity. However, the inclusion of BNNPs while beneficial for thermal enhancement did not contribute significantly to improving the electrical conductivity of the films. In contrast, due to the highly insulating character of BNNPs, a marginal reduction in AC conductivity was observed, especially at higher frequencies. The real part of the AC conductivity corresponds to the charge carrier transport efficiency through the bulk of the material. In CH–CNF–BNNP composites, a slight reduction in the real conductivity with 3% BNNP content was recorded, indicating that BNNP particles act as physical barriers that hinder the long-range transport of charge carriers. This behavior aligns with previous reports where BN-based nanocomposites demonstrated minimal or reduced AC conductivity due to the absence of free charge carriers and

limited electron hopping pathways across the insulating BN network.[56,57] The imaginary part of the AC conductivity, which relates to the dielectric loss and energy dissipation in the material, also decreased with BNNP incorporation. This reduction implies that the BNNP not only restricts the mobility of charge carriers but also reduces dipolar polarization effects and relaxation losses. Such behavior is beneficial for materials targeted toward electronic encapsulation or insulation, where low dielectric loss and strong electrical insulation are required.[58]

Moreover, frequency-dependent measurements demonstrated a decreasing trend in both real and imaginary components of AC conductivity with increasing frequency, as illustrated in Fig. 8(d) and (e). This trend suggests that at higher frequencies, charge carriers are unable to respond to the rapidly oscillating electric field, resulting in diminished conductivity. The decline in AC conductivity upon BNNP incorporation confirms that the composite films become more electrically insulating. These findings underscore the multifunctional nature of BNNPs in tailoring both thermal and dielectric properties without compromising electrical insulation.

3.7. Cole–Cole plot analysis of CNF–CH and CNF–CH–BNNPs

Grain boundaries are typically considered structural imperfections within a crystalline material, often acting as regions of elevated electrical resistance. According to Koop's theory, these boundaries significantly influence the material's overall dielectric and electrical behavior. Therefore, accurately characterizing the dielectric response requires distinguishing the respective contributions of conductive grains and resistive grain boundaries. A widely adopted method for this analysis is the Cole–Cole plot, which effectively separates these contributions. This plot is generated using the dielectric modulus components (M' and M''), derived from the real and imaginary parts of the dielectric constant, using the following equations:[59]

$$M'(\omega) = \frac{\varepsilon'(\omega)}{\varepsilon'(\omega)^2 + \varepsilon''(\omega)^2} \tag{2}$$

$$M''(\omega) = \frac{\varepsilon''(\omega)}{\varepsilon'(\omega)^2 + \varepsilon''(\omega)^2} \tag{3}$$

Fig. 9(a) illustrates the Cole–Cole plots of the imaginary part (M'') *versus* the real part (M') of the electric modulus for pure CNF–CH and BNNP-incorporated CNF–CH films with varying BNNP content (0.5, 1, 2, and 3 wt%). Each plot displays a single semicircular arc, indicating that the resistive grain boundaries have a greater influence on the overall dielectric response than the conductive grains. This highlights a key aspect of the dielectric behavior in these materials. A closer look reveals that the radius of the semicircle increases as BNNP content rises up to 2%, suggesting a decrease in DC conductivity. This enhancement indicates an increased interfacial polarization and relaxation activity, arising from the presence of BN–polymer interfaces, which facilitate dipolar reorientation under the applied electric field. However, at 3% hBN loading, the semicircle radius reduces, which may be due to agglomeration of BN
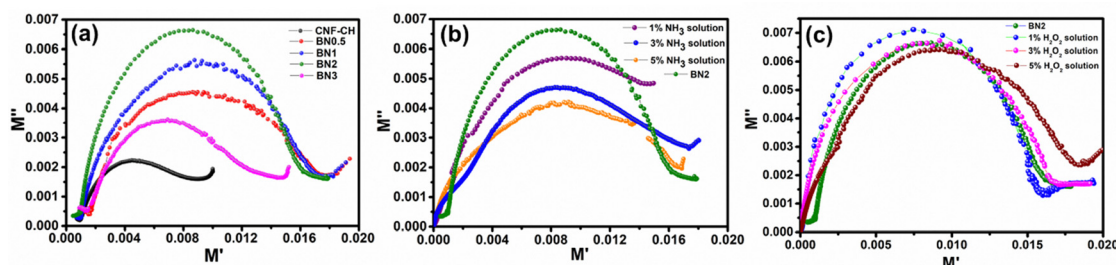
Fig. 9 (a) Cole–Cole plots of different nanocomposite films and sensing performance of the BN2 composite film with (a) NH_3 solution and (c) H_2O_2 solution.

nanoparticles at elevated concentrations as confirmed by the FESEM images, and the tensile strength also decreases, which disrupts the continuity of the polymer network and impedes dipole mobility, resulting in suppressed dielectric relaxation. These findings provide valuable insight into how BNNP loading affects the electrical properties of the composite films.

3.8. NH_3 sensing measurements and mechanism

Based on the Cole–Cole analysis of all the films, the CNF–CH–BNNP film with 2% BNNP loading was selected for sensing applications. The sensing behavior was studied at room temperature (27 °C) by observing changes in the semicircle radius of the Cole–Cole plots upon exposure to different concentrations of NH_3 solution. For this purpose, NH_3 solutions of 1%, 3%, and 5% concentrations (100 μL each) were applied to the surface of 1×1 cm^2 film samples. As shown in Fig. 9(b), the radius of the semicircle in the Cole–Cole plots decreased with NH_3 exposure compared to the control sample, and this decrease became more pronounced with increasing NH_3 concentration. This trend indicates a systematic change in the dielectric response, confirming the film's potential for ammonia sensing applications.[60] The decrease in the radius of the semicircle in the Cole–Cole plot also reflects an enhanced DC conductivity. This behavior suggests that the presence of NH_3 facilitates the electron hopping process within the film, thereby improving its sensing performance.[61]

Response time is a critical parameter for evaluating the performance of a sensor when exposed to a target analyte. In this study, the prepared CNF–CH–BNNP films exhibited an almost instantaneous response upon exposure to NH_3 solution, demonstrating their high sensitivity and quick detection capability. To assess the selectivity of the films, their response to another analyte, H_2O_2 solution, at concentrations of 1%, 3%, and 5% (100 μL each), was also examined. As shown in Fig. 9(c), the response to H_2O_2 was minimal compared to that for NH_3, indicating strong selectivity towards ammonia.

The CH–CNF–BNNP composite film exhibits sensitive dielectric response toward aqueous ammonia due to synergistic interactions between the functional groups present in chitosan and CNF and the high surface area and interfacial polarization capability of BNNPs. The chemical and electronic interactions that occur between the adsorbed analyte and the sensing material play a crucial role in altering its response as a sensor.[62]

Fig. 10(a) presents the sensing mechanism of the sample. Upon exposure to NH_3 in aqueous solution, ammonia undergoes hydrolysis to produce NH_4^+ and OH^- ions. The NH_4^+ ions interact electrostatically with the partially deprotonated amine groups ($-NH_3^+$) of chitosan and $-OH$ groups of cellulose, resulting in increased ionic mobility and rearrangement of local dipoles within the composite matrix.[63] This was further supported by FTIR and I–V analyses of the BN2 film after NH_3 exposure as shown in Fig. S7, which revealed broadening of $-OH/-NH$ bands, confirming the hydrogen bonding interaction between NH_3 and the polymer matrix and the increased current response with increase in NH_3 concentration. This leads to a variation in the dielectric properties of the film, especially under an AC field. Incorporation of BNNP nanoparticles enhances the interfacial polarization due to the dielectric discontinuity at BNNP–polymer and BN–CNF interfaces. The dispersed BNNP acts as a nanobarrier, modulating charge distribution and dielectric relaxation upon NH_3 exposure.[64]

In contrast, the sensing of hydrogen peroxide involves oxidative processes. H_2O_2, being a mild oxidizing agent, can generate hydroxyl radicals (•OH) under aqueous conditions. These radicals may oxidize the amine and hydroxyl functional groups in chitosan and CNFs, leading to chemical modifications such as crosslinking or stiffening of the polymer matrix.[65] These irreversible oxidative interactions alter the dielectric properties less dynamically than ionic NH_3 interactions. As a result, the electric modulus response to H_2O_2 is relatively moderate, with changes in M'–M'' plots being less pronounced. While both analytes induce a detectable shift in the dielectric properties of the BN2 film, ammonia produces a stronger, more reversible dielectric response due to its ionic nature and direct interaction with polar functional groups, making BN2 more sensitive to NH_3 than to H_2O_2.

3.9. Role of BNNPs in enhancing hydrophobicity, chemical resistance, and thermal conductivity: mechanistic insights

The integration of BNNPs into the CH–CNF biopolymer matrix serves as a crucial strategy for imparting multifunctionality, particularly enhancing hydrophobicity, chemical resistance, and thermal conductivity. These enhancements stem not only from the intrinsic properties of BNNPs but also from their ability to interact with the polymer matrix at the nanoscale level, leading to synergistic effects.
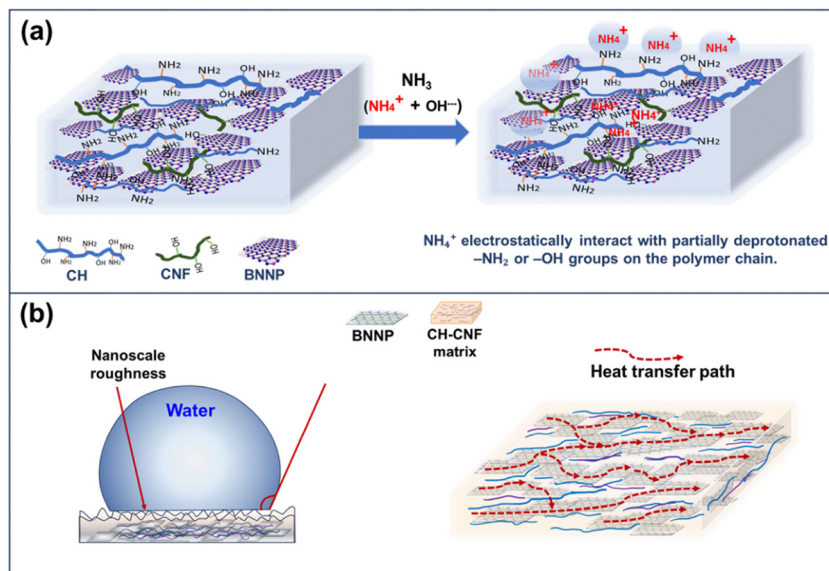
Fig. 10 Schematic representation of the multifunctional role of BNNPs in CH–CNF films: (a) NH_3 sensing *via* electrostatic interaction of NH_4^+ with –NH_2/–OH groups and (b) BNNPs enhance surface roughness for hydrophobicity and form aligned layers enabling efficient in-plane thermal conductivity.

BNNPs are inherently hydrophobic due to the non-polar nature of the B–N covalent bonds and the absence of hydroxyl or carboxyl surface groups. Upon incorporation into the composite, the platelet-like BNNPs orient themselves within the CH–CNF matrix to form micro- and nanoscale topographies that limit surface wetting. As a result, the water contact angle of the films increases significantly from $70.1°$ in CNF-only films to over $125.1°$ in CH–CNF–BNNP films with 3 wt% loading. This enhancement can be explained using the Wenzel and Cassie–Baxter models of surface wetting.[66] The dispersed BNNPs introduce nanoscale roughness (Fig. 10(b)) that promotes air entrapment between water droplets and the film surface, reducing the effective solid–liquid contact area. Furthermore, the low surface energy of BNNPs adds to this effect, leading to a superhydrophobic-like behaviour, particularly at higher concentrations where more surface-exposed BNNPs are present.

One of the primary limitations of chitosan-based films is their susceptibility to hydrolytic degradation in acidic and alkaline environments, primarily due to the presence of amine and hydroxyl groups prone to cleavage.[67] The incorporation of BNNPs mitigates this vulnerability by acting as a physical and chemical barrier within the matrix. Experimental data reveal that after 7-day immersion in 1 M HCl and 1 M NaOH, BNNP-loaded films (BN3) exhibit minimal weight loss ($\sim$2%), whereas pure CH–CNF films undergo significantly higher degradation. Mechanistically, BNNPs hinder the diffusion of acidic or basic media through the polymer network by increasing the tortuosity of the permeation path. This barrier effect is amplified by the layered structure of BNNPs, which mimics a brick wall configuration, dispersing aggressive chemical attacks across broader surface areas and minimizing localized degradation. The internal structure of BN1 and BN2 films clearly displays a more compact and layered internal structure,

indicating a uniform distribution of BNNPs throughout the CH–CNF matrix, as evidenced in the SEM cross sectional image, supporting the idea that BNNPs are evenly dispersed in a layered fashion within the film visually reinforcing the brick-wall analogy. Moreover, the inert and chemically stable nature of BNNPs resists reaction or dissolution under both acidic and basic conditions, contributing to the overall robustness of the composite.

The poor thermal conductivity of conventional biopolymers ($\sim$0.1 W m^{-1} °C^{-1}) severely limits their utility in applications such as flexible electronics and thermally resistant coatings. Incorporating BNNPs leads to a significant increase in thermal conductivity, reaching values up to 0.68 W m^{-1} °C^{-1} in the BN3 composite at 20 °C. This enhancement originates from the high intrinsic thermal conductivity of bulk h-BN (200–400 W m^{-1} °C^{-1}) and the efficient phonon transport pathways it introduces. At the molecular level, thermal conductivity in polymer nanocomposites is governed by phonon transport efficiency. BNNPs, with their ordered crystalline lattice and strong in-plane B–N bonds, act as efficient phonon conductors.[40] When uniformly dispersed within the matrix, they reduce phonon scattering events at grain boundaries and interfaces, facilitating more direct thermal transport as shown in Fig. 10(b). The surface SEM images in Fig. 5(c)–(f) reveal the increasing presence and uniform dispersion of BNNPs across the film surface as the concentration increases. More importantly, the cross-sectional images (Fig. 5(c′)–(f′)) provide visual evidence of layered and horizontal alignment of BNNPs within the film, where BNNPs act like stacked flat tiles between polymer chains. From this configuration, it is found that the improvement in thermal conductivity is linked to three interconnected mechanisms. Firstly, the uniformly dispersed BNNPs make thermally conductive bridges throughout the

CH–CNF matrix. These bridges create percolating phonon pathways that bypass the intrinsically insulating polymer chains. Second, the high interfacial adhesion between BNNPs, CNFs, and the chitosan matrix mediated through hydrogen bonding and surface compatibility reduces interfacial phonon scattering and makes phonon coupling across the filler matrix boundaries. The fibrous and linked structure of the CNFs, further stabilized the dispersion of BNNPs, which makes it easier for heat to pass through them. Third, the partial in-plane alignment of BNNPs reduces the number of phonon reflection interfaces and makes it easier for directional heat flow, which explains the observed increase in both thermal diffusivity and conductivity at higher BNNP loadings (BN2 and BN3).[55,68]

4. Conclusion

This study demonstrates an effective and sustainable approach for fabricating multifunctional bio-composite films through incorporating the combination of BNNPs and CNFs into a CH matrix. The resulting CH–CNF–BNNP composite films show remarkable improvements in mechanical strength, hydrophobicity, thermal conductivity, and chemical resistance. A progressive increase in BNNP loading leads to improvement in tensile strength, thermal conductivity and hydrophobic nature due to enhanced interfacial interaction and high inherent properties of BNNPs. Among all compositions, the film with 2 wt% BNNPs (BN2) exhibited the most balanced and superior performance, achieving a tensile strength of 46.3 MPa ($\sim$82% improvement relative to CH–CNF), a high contact angle of 117.1°, and a thermal conductivity of 0.68 W m^{-1} °C^{-1} at 20 °C. These enhancements were attributed to the synergistic interaction between CNFs and BNNPs, where CNFs improved network integrity and BNNPs served as thermally conductive lamellae with low surface energy, thereby enhancing hydrophobicity and reducing water affinity. Chemical resistance studies confirmed the composite's structural stability in acidic and alkaline environments, particularly at 3% BNNP loading concentrations, showing a minimal weight loss of 1.8% in base and 2.8% in acid after 24 h.

Thermal analysis further revealed significant improvements in heat dissipation, attributed to the establishment of continuous phonon transport channels within the CH–CNF–BNNP matrix. The BN3 composite demonstrates the highest thermal conductivity, reaching up to 0.75 W m^{-1} °C^{-1} at 80 °C, primarily due to the high intrinsic thermal conductivity of BNNPs and their uniform dispersion within the CH–CNF matrix, which facilitates more efficient phonon transport pathways. The films maintained excellent electrical insulation, making them suitable for dielectric and flexible electronic applications. Furthermore, the dielectric response of the BN2 film toward NH$_3$ exposure indicated high sensitivity and selectivity, as evident from the Cole–Cole plot analysis. This behaviour was attributed to the modulation of interfacial polarization and electrostatic interactions between NH$_4^+$ ions and the polymer matrix. Overall, the CH–CNF–BNNP bio-composite films effectively overcome many of the inherent limitations associated with conventional biopolymer films, offering an environmentally benign, mechanically robust, and thermally stable material platform suitable for sustainable packaging, flexible electronics, protective coatings, and chemical sensing applications.

Author contributions

The manuscript was written through the contribution of all the authors. All authors have given approval to the final version of the manuscript.

Conflicts of interest

The authors declare no conflict of interest.

Data availability

The datasets used and/or analyzed during the current study are available from the corresponding author upon reasonable request.

The data supporting this article have been included as part of the supplementary information (SI). It contains FTIR of exfoliated BNNP, FTIR spectrum of bulk BN and as exfoliated BNNP, FE-SEM and TEM of bulk *h*-BN and as exfoliated BNNP, FTIR and FE-SEM of acid and base treated CH–CNF–BNNP. See DOI: https://doi.org/10.1039/d5ma00702j.

Acknowledgements

References

1 L. Yu, K. Dean and L. Li, *Prog. Polym. Sci.*, 2006, **31**, 576–602.
2 M. Mangal, C. V. Rao and T. Banerjee, *Polym. Int.*, 2023, **72**, 984–996.
3 A. George, M. R. Sanjay, R. Srisuk, J. Parameswaranpillai and S. Siengchin, *Int. J. Biol. Macromol.*, 2020, **154**, 329–338.
4 Y. Xie, S. Gao, D. Zhang, C. Wang and F. Chu, *Resour. Chem. Mater.*, 2023, **2**, 223–230.
5 A. Chakraborty, P. Ghalsasi and P. Radha, *J. Inorg. Organomet. Polym.*, 2023, **33**, 1119–1133.
6 S. A. Marand, H. Almasi and N. A. Marand, *Int. J. Biol. Macromol.*, 2021, **190**, 667–678.

7 B. Boro, R. S. Warkhedkar, R. Sonkar and D. Chowdhury, *Chemistry Select*, 2025, **10**, e202405895.

8 M. Mahardika, N. Masruchin, D. Amelia, R. A. Ilyas, A. A. Septevani, E. Syafri, N. Hastuti, M. Karina, M. A. Khan, B.-H. Jeon and N. H. Sari, *RSC Adv.*, 2024, **14**, 23232–23239.

9 E. Jamróz, P. Kulawik and P. Kopel, *Polymers*, 2019, **11**, 675.

10 N. Kaur, A. Arya, R. Kumar, J. Kaur, N. Savita, N. Khattar, P. K. Diwan and A. Sharma, *Mater. Sci. Eng., B*, 2023, **293**, 116495.

11 S. J. Peighambardoust, S. H. Peighambardoust, N. Pournasir and P. M. Pakdel, *Food Packag. Shelf Life.*, 2019, **22**, 100420.

12 K. Liang, E. M. Spiesz, D. T. Schmieden, A.-W. Xu, A. S. Meyer and M.-E. Aubin-Tam, *ACS Nano*, 2020, **14**, 14731–14739.

13 R. O. Medupin, O. K. Abubakre, A. S. Abdulkareem, R. A. Muriana and A. S. Abdulrahman, *Sci. Rep.*, 2019, **9**, 20146.

14 B. Mohan, U. Boruah, R. Sonkar, N. J. Mondal and D. Chowdhury, *Part. Part. Syst. Charact.*, 2025, **42**, 2400156.

15 H. Fang, S.-L. Bai and C. P. Wong, *Compos. Commun.*, 2016, **2**, 19–24.

16 K. Zhang, Y. Feng, F. Wang, Z. Yang and J. Wang, *J. Mater. Chem. C*, 2017, **5**, 11992–12022.

17 C. Pan, K. Kou, Q. Jia, Y. Zhang, G. Wu and T. Ji, *Composites, Part B*, 2016, **111**, 83–90.

18 B. Yu, W. Xing, W. Guo, S. Qiu, X. Wang, S. Lo and Y. Hu, *J. Mater. Chem. A*, 2016, **4**, 7330–7340.

19 A. Morshed, F. Lin, H. Wu, Z. Xing, S. Jiao, M. M. Hasan and Z. Jiang, *Nanoscale Adv.*, 2025, **7**, 1972–1988.

20 K. Oesef, E. D. Cranston and Y. Abdin, *Mater. Des.*, 2024, **247**, 113417.

21 J. Zeng, Z. Zeng, Z. Cheng, Y. Wang, X. Wang, B. Wang and W. Gao, *Sci. Rep.*, 2021, **11**, 11918.

22 Y. Okuda, E. Kido, K. Hirota and T. Mizutani, *ACS Appl. Polym. Mater.*, 2023, **5**, 8082–8088.

23 D. França, L. M. Angelo, C. F. Souza and R. Faez, *ACS Appl. Polym. Mater.*, 2021, **3**, 3227–3237.

24 X. Xu, F. Liu, L. Jiang, J. Y. Zhu, D. Haagenson and D. P. Wiesenborn, *ACS Appl. Mater. Interfaces*, 2013, **5**, 2999–3009.

25 R. Masoodi, R. F. El-Hajjar, K. M. Pillai and R. Sabo, *Mater. Des.*, 2011, **36**, 570–576.

26 B. Joseph, V. K. Sagarika, C. Sabu, N. Kalarikkal and S. Thomas, *J. Bioresour. Bioprod.*, 2020, **5**, 223–237.

27 Z. Lu, H. Zhang, M. Toivakka and C. Xu, *Int. J. Biol. Macromol.*, 2024, **267**, 131490.

28 X. Nie, Y. Xie, X. Ding, L. Dai, F. Gao, W. Song, X. Li, P. Liu, Z. Tan, H. Shi, C. Lai, D. Zhang and Y. Lai, *Carbohydr. Polym.*, 2024, **334**, 122068.

29 J. Joy, E. George, P. Haritha, S. Thomas and S. Anas, *J. Polym. Sci.*, 2020, **58**, 3115–3141.

30 W. Shao, X. Zhang, X. Liang, W. Tao, M. Ma, S. Chen, Y. Shi, H. He, Y. Zhu and X. Wang, *ACS Appl. Mater. Interfaces*, 2024, **16**, 42674–42686.

31 G. Yang, X. Zhang, Y. Shang, P. Xu, D. Pan, F. Su, Y. Ji, Y. Feng, Y. Liu and C. Liu, *Compos. Sci. Technol.*, 2020, **201**, 108521.

32 K. Li, S. Jin, H. Chen and J. Li, *Composites, Part B*, 2019, **171**, 222–234.

33 Y. Ogawa, K. Azuma, H. Izawa, M. Morimoto, K. Ochi, T. Osaki, N. Ito, Y. Okamoto, H. Saimoto and S. Ifuku, *Int. J. Biol. Macromol.*, 2017, **104**, 1882–1889.

34 A. O. Silva, R. S. Cunha, D. Hotza and R. A. F. Machado, *Carbohydr. Polym.*, 2021, **272**, 118472.

35 K. Behera, M. Kumari, Y.-H. Chang and F.-C. Chiu, *Int. J. Biol. Macromol.*, 2021, **186**, 135–144.

36 L. Dai, Y. Geng, X. Ding, Z. Zhang, C. Lai, D. Zhang, C. Xia and Y. Lai, *Carbohydr. Polym.*, 2025, **366**, 123869.

37 C. Huang, X. Qian and R. Yang, *Mater. Sci. Eng., R*, 2018, **132**, 1–22.

38 N. T. Dintcheva, *Polymer*, 2024, **306**, 127136.

39 Z. P. Mathew, G. K. Shamnamol, K. P. Greeshma and S. John, *Corros. Commun.*, 2023, **9**, 36–43.

40 V. Guerra, C. Wan and T. McNally, *Prog. Mater. Sci.*, 2018, **100**, 170–186.

41 A. K. Sonker, M. H. Tran, N. Park, G. S. Das, H. Mahajan, T. H. Lee and T. Kim, *ACS Omega*, 2025, **10**, 1853–1861.

42 M. G. Rasul, A. Kiziltas, B. Arfaei and R. Shahbazian-Yassar, *npj 2D Mater. Appl.*, 2021, **5**, 56.

43 N. Mittal, G. Kedawat, N. Kanika, S. Gupta and B. K. Gupta, *ChemistrySelect*, 2020, **5**, 12564–12569.

44 Z. Du, X. Zeng, M. Zhu, A. Kanta, Q. Liu, J. Li and L. B. Kong, *Ceram. Int.*, 2018, **44**, 21461–21469.

45 C. Huang, C. Chen, X. Ye, W. Ye, J. Hu, C. Xu and X. Qiu, *J. Mater. Chem. A*, 2013, **1**, 12192.

46 L. Ravindran, M. S. Sreekala and S. Thomas, *Int. J. Biol. Macromol.*, 2019, **131**, 858–870.

47 W. Chen, H. Yu, Y. Liu, Y. Hai, M. Zhang and P. Chen, *Cellulose*, 2011, **18**, 433–442.

48 A. Mtibe, L. Z. Linganiso, A. P. Mathew, K. Oksman, M. J. John and R. D. Anandjiwala, *Carbohydr. Polym.*, 2014, **118**, 1–8.

49 N. S. Syazwani, M. N. E. Efzan, C. K. Kok and M. J. Nurhidayatullaili, *J. Build. Mater. Eng.*, 2021, **48**, 103744.

50 M.-C. Popescu, C.-M. Popescu, G. Lisa and Y. Sakata, *J. Mol. Struct.*, 2011, **988**, 65–72.

51 A. Grząbka-Zasadzińska, T. Amietszajew and S. Borysiak, *J. Therm. Anal. Calorim.*, 2017, **130**, 143–154.

52 N. E. Mushi, S. Utsel and L. A. Berglund, *Front. Chem.*, 2014, **2**, 99.

53 E. Aigaje, A. Riofrio and H. Baykara, *Polymers*, 2023, **15**, 1219.

54 T. Stern and G. Marom, *J. Compos. Sci.*, 2024, **8**, 395.

55 G. Yang, X. Zhang, D. Pan, W. Zhang, Y. Shang, F. Su, Y. Ji, C. Liu and C. Shen, *ACS Appl. Mater. Interfaces*, 2021, **13**, 32286–32294.

56 J. Chen, X. Huang, Y. Zhu and P. Jiang, *Adv. Funct. Mater.*, 2016, **27**, 1704754.

57 X. Meng, J. Zhang, J. Ma, Y. Li, Z. Chen, S. Liu, T. Chen, Y. Zhang, X. Jiang and S. Zhu, *Composites, Part A*, 2020, **138**, 106089.

58 J. Sun, Y. Yao, X. Zeng, G. Pan, J. Hu, Y. Huang, R. Sun, J. Xu and C. Wong, *Adv. Mater. Interfaces*, 2017, **4**, 1700563.

59 M. P. Ghosh, R. Sonkar, G. Phukan, J. P. Borah and D. Chowdhury, *RSC Adv.*, 2025, **15**, 12964–12981.

60 A. Jain, S. K. Gautam and S. Panda, *Phys. Scr.*, 2023, **98**, 095909.

61 X. Yuan, A. Sha, S. Huang, H. Zhao, X. Chen, Y. Zhang and S. Guo, *J. Alloys Compd.*, 2021, **890**, 161903.

62 R. Sonkar, M. P. Ghosh, S. Thakur, E. Saikia and D. Chowdhury, *Mater. Chem. Phys.*, 2025, 130578.

63 I. Tagliaro, G. Musile, P. Caricato, R. M. Dorizzi, F. Tagliaro and C. Antonini, *Polymers*, 2023, **15**, 4238.

64 M. Yang, H. Zhao, D. He, C. Hu, H. Chen and J. Bai, *Materials*, 2017, **10**, 741.

65 J. Li, P. Li, B. Zhang, J. Fang, W. Zhong and F. Ma, *Int. J. Biol. Macromol.*, 2024, **262**, 130260.

66 A. Giacomello, S. Meloni, M. Chinappi and C. M. Casciola, *Langmuir*, 2012, **28**, 10764–10772.

67 P. Cazón and M. Vázquez, *Environ. Chem. Lett.*, 2019, **18**, 257–267.

68 Y. Liu, W. Gong, X. Liu, Y. Fan, A. He and H. Nie, *Polymers*, 2024, **16**, 1169.